

STUDY OF SWIFT/BAT SELECTED LOW-LUMINOSITY ACTIVE GALACTIC NUCLEI OBSERVED WITH SUZAKU

TAIKI KAWAMURO¹, YOSHIHIRO UEDA¹, FUMIE TAZAKI², YUICHI TERASHIMA³, RICHARD MUSHOTZKY⁴,
Draft version April 28, 2016

ABSTRACT

We systematically analyze the broadband (0.5–200 keV) X-ray spectra of hard X-ray (> 10 keV) selected local low-luminosity active galactic nuclei (LLAGNs) observed with *Suzaku* and *Swift*/BAT. The sample consists of ten LLAGNs detected with *Swift*/BAT with intrinsic 14–195 keV luminosities smaller than 10^{42} erg s^{−1} available in the *Suzaku* archive, covering a wide range of the Eddington ratio from 10^{-5} to 10^{-2} . The overall spectra can be reproduced with an absorbed cut-off power law, often accompanied by reflection components from distant cold matter, and/or optically-thin thermal emission from the host galaxy. In all objects, relativistic reflection components from the innermost disk are not required. Eight objects show a significant narrow iron-K α emission line. Comparing their observed equivalent widths with the predictions from the Monte-Carlo based torus model by Ikeda et al. (2009), we constrain the column density in the equatorial plane to be $\log N_{\text{H}}^{\text{eq}} > 22.7$ or the torus half opening angle $\theta_{\text{oa}} < 70^\circ$. We infer that the Eddington ratio (λ_{Edd}) is a key parameter that determines the torus structure of LLAGNs: the torus becomes large at $\lambda_{\text{Edd}} \gtrsim 2 \times 10^{-4}$, whereas at lower accretion rates it is little developed. The luminosity correlation between the hard X-ray and mid-infrared (MIR) bands of the LLAGNs follows the same one as for more luminous AGNs. This implies that other mechanisms than AGN-heated dust are responsible for the MIR emission in low Eddington ratio LLAGNs.

Subject headings: galaxies: active – galaxies: individual (NGC 2655, NGC 3718, NGC 3998, NGC 4102, NGC 4138, NGC 4258, NGC 4395, NGC 4941, NGC 5273, NGC 5643) – X-rays: galaxies

1. INTRODUCTION

Active galactic nuclei (AGNs) emit intense X-ray radiation by converting the gravitational energy of matter accreted onto the supermassive black holes (SMBHs). According to the so-called AGN unified model (Antonucci 1993), the central engine is obscured by a dusty torus, which affects the observed X-ray spectrum via photoelectric absorption and Compton reflection. In addition, a relativistically blurred reflection component from the innermost accretion disk would be expected when the disk is extended down to a vicinity of the SMBH. Hence, observations of broadband X-ray spectra of AGNs are useful to investigate their structure including the torus and accretion disk.

Low-luminosity AGNs (LLAGNs), which we define by their low X-ray luminosities in the 14–195 keV band ($L_{\text{X}} < 10^{42}$ erg s^{−1}), are important objects to understand the evolution of AGNs. LLAGNs contain two extreme types of AGNs: those with a small SMBH mass and a high mass-accretion rate (i.e., with a high Eddington ratio), and those with a large SMBH mass and a low mass-accretion rate (a low Eddington ratio). The former type is expected in the early growing phase of a SMBH, whereas the latter corresponds to the fading phase of an

AGN into a quiescent SMBH. Broadband X-ray studies of LLAGNs have been limited, however, because of their low fluxes even in the local Universe (Kawamuro et al. 2013).

Theories and observations suggest that LLAGNs are not a simple scaled-down version of luminous AGNs in terms of their nucleus structure. When the accretion rate falls below a critical level, it is predicted that the state of the inner accretion disk changes from the standard accretion disk (Shakura & Sunyaev 1973) to an optically-thin radiatively inefficient accretion flow (RIAF; Narayan et al. 1998; Quataert 2001). Studies of spectral energy distributions (SEDs) from the radio to X-ray bands showed that the standard disk is truncated at a radius much larger than a few Schwarzschild radii (e.g., Nemmen et al. 2011; Mason et al. 2012). This is supported by the lack of the big blue bump in LLAGNs, which arises from the thermal emission from the inner standard disk (e.g., Ho 2008). Moreover, most of LLAGNs do not show a broad iron-K α line feature, suggesting that the standard disk does not extend to the inner most region around the SMBH, except for some LLAGNs (e.g., NGC 4051; Guainazzi et al. 1996). Also, Gu & Cao (2009) found a negative correlation between the X-ray photon index and Eddington ratio for low Eddington ratio AGNs ($\lambda_{\text{Edd}} < 0.01$), whereas the positive one for luminous AGNs was reported by Shemmer et al. (2008). Gu & Cao (2009) suggested that the negative correlation can be explained with a RIAF model. For the detailed investigations of the broad iron line feature and continuum components, broadband X-ray spectra are highly important.

¹ Department of Astronomy, Kyoto University, Kyoto 606-8502, Japan

² Mizusawa VLBI Observatory, National Astronomical Observatory of Japan, Osawa, Mitaka, Tokyo 181-8588, Japan

³ Department of Physics, Ehime University, Matsuyama 790-8577, Japan

⁴ Department of Astronomy, University of Maryland, CollegePark, MD 20742-2421, USA

X-ray surveys showed that the absorbed AGN fraction, which reflects the torus covering factor, decreases with X-ray luminosity (e.g., Ueda et al. 2003, 2014; Della Ceca et al. 2008; Hasinger 2008; Merloni et al. 2014; Buchner et al. 2015). These results would be consistent with receding torus models (e.g., Lawrence 1991), where the inner wall of the torus recedes with luminosity by keeping its scale-height more constant. However, recent surveys have found evidence that the absorbed AGN fraction decreases towards lower X-ray luminosities from a peak around $L_X \sim 10^{42-43}$ erg s $^{-1}$ (e.g., Beckmann et al. 2009; Burlon et al. 2011; Brightman & Nandra 2011). These facts suggest that, at low luminosities, other physical mechanisms than AGN radiation must be responsible to determine the torus structure.

Main goals of this paper are (1) to best constrain the X-ray spectral properties of LLAGNs by taking advantage of their “broadband” (0.5–200 keV) data observed with *Suzaku* and *Swift*/BAT, (2) to reveal the nuclear structure including the torus and accretion disk, and (3) to find key parameters that determine them. Most of previous studies are limited to soft energy bands below ~ 10 keV (e.g., González-Martín et al. 2009). From the *Swift*/BAT 70-month catalog (Baumgartner et al. 2013), we select all ten LLAGNs ($\log L_X < 42$ in the 14–195 keV band) whose *Suzaku* archival data are public. We exclude NGC 4051, which is known to exhibit large spectral variation among different epochs (e.g., Guainazzi et al. 1996; Pounds et al. 2004; Terashima et al. 2009). This paper is organized as follows. Section 2 describes the details of the observation and the overview of the data. We show the results of the spectral analysis in Section 3. The discussion and conclusions are presented in Sections 4 and 5, respectively. Unless otherwise noted, all errors are quoted at the 90% confidence level for a single parameter of interest.

2. OBSERVATION AND DATA REDUCTION

2.1. Observations

The basic information of our targets is summarized in Table 1. The distances are taken from the literature or are calculated from the redshift. The black hole masses are compiled from the literature or are calculated from the stellar velocity dispersion by using the relation of Gültekin et al. (2009). *Suzaku* (Mitsuda et al. 2007) observations of our targets were performed with exposures of ~ 40 –80 ksec. Table 2 gives the observation log.

Suzaku carries X-ray CCD cameras that cover the energy range below ~ 10 keV called the X-ray Imaging Spectrometer (XIS), and a non-imaging instrument sensitive to hard X-rays above ~ 15 keV called the hard X-ray Detector (HXD). Two front-illuminated XISs (FI-XISs; XIS-0 and XIS-3) and one back-illuminated XIS (BI-XIS; XIS-1) were available during the observations. All targets were too faint above ~ 50 keV to be detected with HXD/GSO. HXD/PIN was not operated during the observation of NGC 2655, and no HXD/PIN data of NGC 4138 were available because of a telemetry saturation problem. NGC 2655, NGC 3998, NGC 4258, NGC 4941, and NGC 5273 were observed at the XIS nominal position, whereas the others were observed at the HXD nominal position.

FTOOLS (version 6.15.1) and XSPEC (version 12.8.1.g) are used for the data reduction and spectral analysis. The CALDB released on 2015 Jan 5 are utilized. We reprocess the XIS event files according to the ABC guide and extract source events from a circular region centered on the target centroid. The background events are taken from an off-source region within the XIS field-of-view. The FI-XISs data are merged to increase the signal-to-noise ratio. We utilize the cleaned event files of HXD/PIN provided by the *Suzaku* team. To reproduce the background spectra, we utilize the “tuned” Non X-ray background model (Fukazawa et al. 2009) and the Cosmic X-ray background spectrum simulated by assuming the model given in Gruber et al. (1999). From eight targets except NGC 2655 and NGC 4138, we detect significant signals with HXD/PIN well above the systematic uncertainties in the Non X-ray background model (1% for the exposure time above 40 ksec; Fukazawa et al. 2009). In the spectral analysis, we also use the *Swift*/BAT spectra averaged for 70 months (Baumgartner et al. 2013).

2.2. Light Curves

Figure 1 shows the background-subtracted light curves of our sample in the 2–10 keV band (XIS-0+XIS-3). The bin size is set to 5760 sec (the orbital period of *Suzaku*) to exclude any modulations that depend on the orbital phase. Strong time variability is seen in NGC 4395 and NGC 5273. To quantify it, we calculate the mean fractional variation (F_{var}) defined in equation (3) of Rodríguez-Pascual et al. (1997):

$$F_{\text{var}} = \sqrt{\frac{S^2 - \overline{\sigma}^2}{\bar{r}^2}},$$

where

$$S^2 = \frac{1}{N-1} \sum_{i=1}^N (r_i - \bar{r})^2$$

and

$$\overline{\sigma}^2 = \frac{1}{N} \sum_{i=1}^N \sigma_i^2.$$

Here, for the sample size N , r and \bar{r} is an observed flux and the mean value, respectively, while σ an error. Larger F_{var} means that the object is more variable. Also, by fitting a constant flux model to the light curves, we calculate the probability of obtaining the observed data (p-value) based on chi-square distribution. F_{var} and p-values of the 2–10 keV light curves are summarized in Table 3. Judging from $F_{\text{var}} > 0.3$ and p-value < 0.01 , NGC 4395 and NGC 5273 were highly variable. This would reflect the small spatial scale of the X-ray emitting region inferred from their low SMBH masses ($M_{\text{BH}} < 5 \times 10^6 M_{\text{sol}}$, where M_{sol} is the solar mass). Although the SMBH mass of NGC 5643 is also low, its variability may be suppressed due to heavy obscuration of the direct transmitted emission (Guainazzi et al. 2004; Matt et al. 2013). As we will discuss in Section 3.2, in these low-mass LLAGNs the flux of the reflection component from the torus follows that of the primary emission on time scales shorter than 70 months.

TABLE 1
BASIC INFORMATION OF THE TARGETS

Target Name (1)	SWIFT ID (2)	Type (3)	R.A.(J2000) (4)	Decl. (J2000) (5)	Redshift (6)	D (7)	$\log M_{\text{BH}}/M_{\text{sol}}$ (8)	Ref. (9)
NGC 2655	J0856.0+7812	Seyfert 2	08h55m37.7s	+78d13m23s	4.670×10^{-3}	24.4	$7.7^{+0.1}_{-0.2}$	(1,1)
NGC 3718	J1132.7+5301	XBONG	11h32m34.9s	+53d04m05s	3.312×10^{-3}	17.0	8.0 ± 0.3	(1,2)
NGC 3998	J1157.8+5529	Seyfert 1/LINER	11h57m56.1s	+55d27m13s	3.496×10^{-3}	19.4	8.9 ± 0.1	(2,3)
NGC 4102	J1206.2+5243	LINER	12h06m23.0s	+52d42m40s	2.823×10^{-3}	19.1	$7.9^{+0.1}_{-0.2}$	(3,1)
NGC 4138	J1209.4+4340	Seyfert 1.9	12h09m29.8s	+43d41m07s	2.962×10^{-3}	15.9	$7.2^{+0.1}_{-0.2}$	(4,1)
NGC 4258	J1219.4+4720	Seyfert 1.9/LINER	12h18m57.5s	+47d18m14s	1.494×10^{-3}	7.6	$7.61^{+0.02}_{-0.01}$	(5,4)
NGC 4395	J1202.5+3332	Seyfert 1.9	12h25m48.9s	+33d32m49s	1.064×10^{-3}	3.9	$5.6^{+0.2}_{-0.1}$	(3,5)
NGC 4941	J1304.3-0532	Seyfert 2	13h04m13.1s	-05d33m06s	3.696×10^{-3}	19.7	6.9 ± 0.3	(2,6)
NGC 5273	J1341.9+3537	Seyfert 1.9	13h42m08.3s	+35d39m15s	3.619×10^{-3}	13.1	$6.7^{+0.1}_{-0.2}$	(2,7)
NGC 5643	J1432.8-4412	Seyfert 2	14h32m40.7s	-44d10m28s	3.999×10^{-3}	16.9	6.3 ± 0.4	(1,6)

NOTE. — Columns: (1) Galaxy name. (2) *Swift* ID. (3) Galaxy type taken from the *Swift*/BAT 70-month catalog (Baumgartner et al. 2013). (4)-(6) Position and redshift taken from the NASA/IPAC Extragalactic Database. (7) Luminosity distance in units of Mpc. (8) Black hole mass with 1σ error. (9) References for distances and black hole masses.

References for distances.

(1) Tully (1988), (2) Theureau et al. (2007), (3) Tully et al. (2009), (4) Springob et al. (2009), (5) Humphreys et al. (2013)

References for black hole masses.

(1) Mass calculated with the M_{BH} -stellar velocity dispersion relation derived by Gültekin et al. (2009), where the stellar dispersion is taken from Ho et al. (2009). (2) Markakis et al. (2015), (3) Walsh et al. (2012), (4) Herrnstein et al. (1999), (5) den Brok et al. (2015), (6) Davis et al. (2014), (7) Bentz et al. (2014).

TABLE 2
OBSERVATION LOG

Target Name (1)	Start Date of Obs. (UT) (2)	Obs. ID (3)
NGC 2655	2014 May 12	709003010
NGC 3718	2009 Oct. 24	704048010
NGC 3998	2014 May 03	709002010
NGC 4102	2009 May 30	704057010
NGC 4138	2009 Nov. 02	704047010
NGC 4258	2010 Nov. 11	705051010
NGC 4395	2007 June 02	702001010
NGC 4941	2012 June 22	707001010
NGC 5273	2013 July 16	708001010
NGC 5643	2007 Aug. 19	702010010

NOTE. — Columns: (1) Galaxy name. (2) Observation start date. (3) *Suzaku* observation ID.

TABLE 3
VARIABILITY IN THE 2–10 keV LIGHT CURVES

Target Name (1)	F_{var} (2)	p-value (3)
NGC 2655	0.064	0.02
NGC 3718	0.031	0.08
NGC 3998	0.003	0.40
NGC 4102	0.138	0.07
NGC 4138	0.040	0.24
NGC 4258	0.083	< 0.01
NGC 4395	0.424	< 0.01
NGC 4941	0.090	0.02
NGC 5273	0.303	< 0.01
NGC 5643	0.106	0.06

NOTE. — Columns: (1) Galaxy name. (2) Fractional variability. (3) Probability of obtaining the observed light curve at constant flux.

3. ANALYSIS AND RESULTS

3.1. Broadband Spectral Analysis

We simultaneously analyze the X-ray spectra of the FI-XISs, BI-XIS, HXD/PIN, and *Swift*/BAT, which cover the 1–12 keV, 0.5–8 keV, 14–60 keV, and 15–200 keV bands, respectively. We exclude the 1.7–1.9 keV band of the XIS spectra to avoid systematic uncertainties of the energy response around the Si K-edge region. The cross-normalization factor of the HXD/PIN spectrum to the FI-XISs one is set to 1.16 (1.18) for the XIS (HXD) nominal position observation, and that of the BI-XIS spectrum is allowed to vary.

On the basis of the previous works (Tazaki et al. 2013; Kawamuro et al. 2013), we start with a base-line model,

$$\text{constant} * \text{zphabs} * \text{zpowerlw} * \text{zhighcut} \\ + \text{constant} * \text{zpowerlw} * \text{zhighcut} + \text{pexrav} + \text{zgauss}$$

in the XSPEC terminology. This model includes absorbed primary X-ray emission (i.e., a cut-off power law), a scattered component, and a reflection continuum from distant cold matter accompanied with a narrow iron- $K\alpha$ line. Optically-thin thermal emission from the host galaxy (**apec** in XSPEC) and other emission/absorption lines (**zgauss**) are also added if they are significantly required with a confidence level above 90% in terms of $\Delta\chi^2$. Because it is difficult to determine the cut-off energy from our data, we fix it at 300 keV, a typical value measured in nearby AGNs (Dadina 2008). The first **constant** factor, N_{XIS} , is applied to the primary power-law component in the *Suzaku* spectra to absorb possible time variability between the *Suzaku* (one epoch) and *Swift*/BAT (averaged for 70 months) observations. The second **constant** term represents the scattered fraction, f_{scatt} . As a reflection component from the torus, we employ the **pexrav** model,

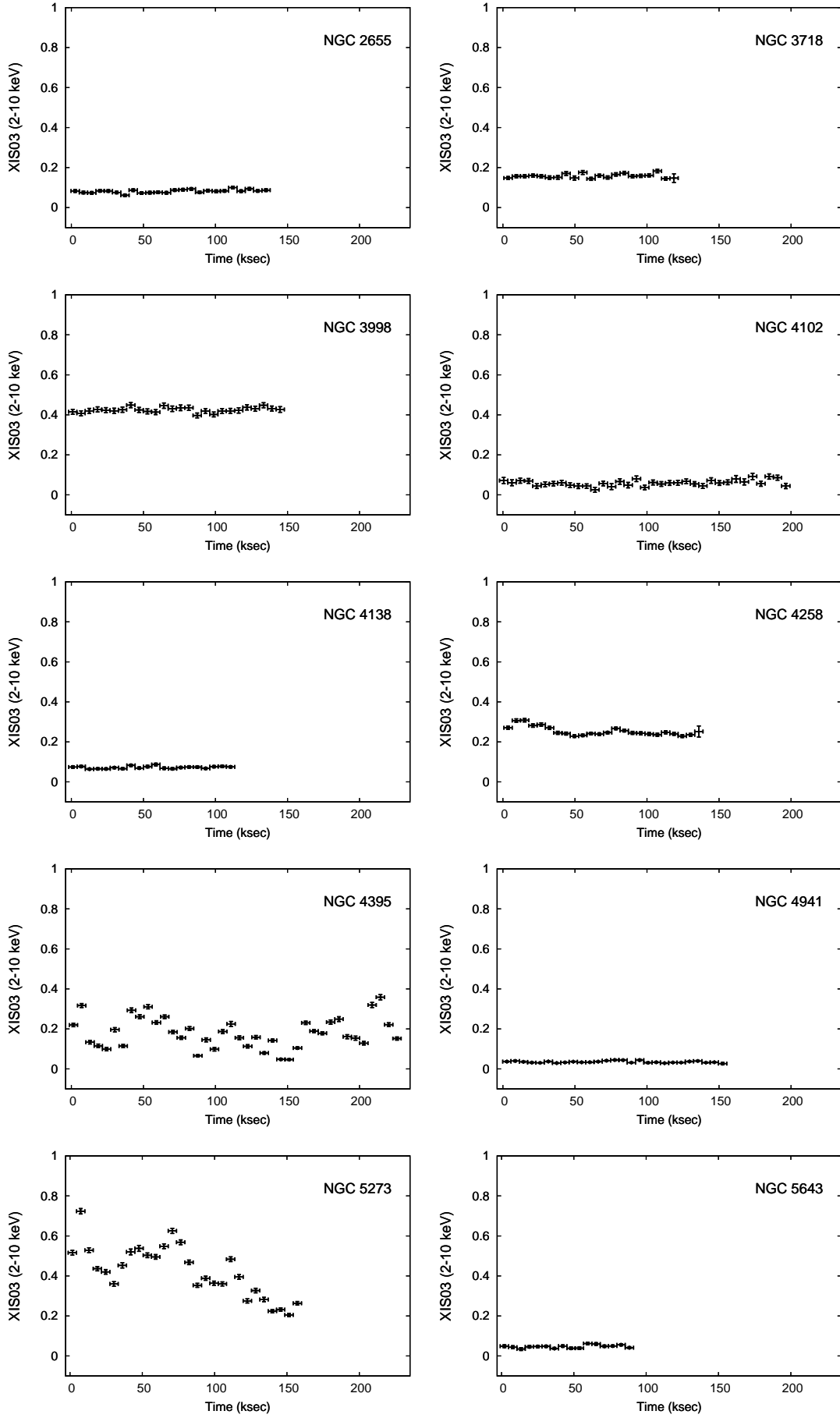


FIG. 1.— Count-rate light curves in the 2–10 keV band obtained with FI-XISs.

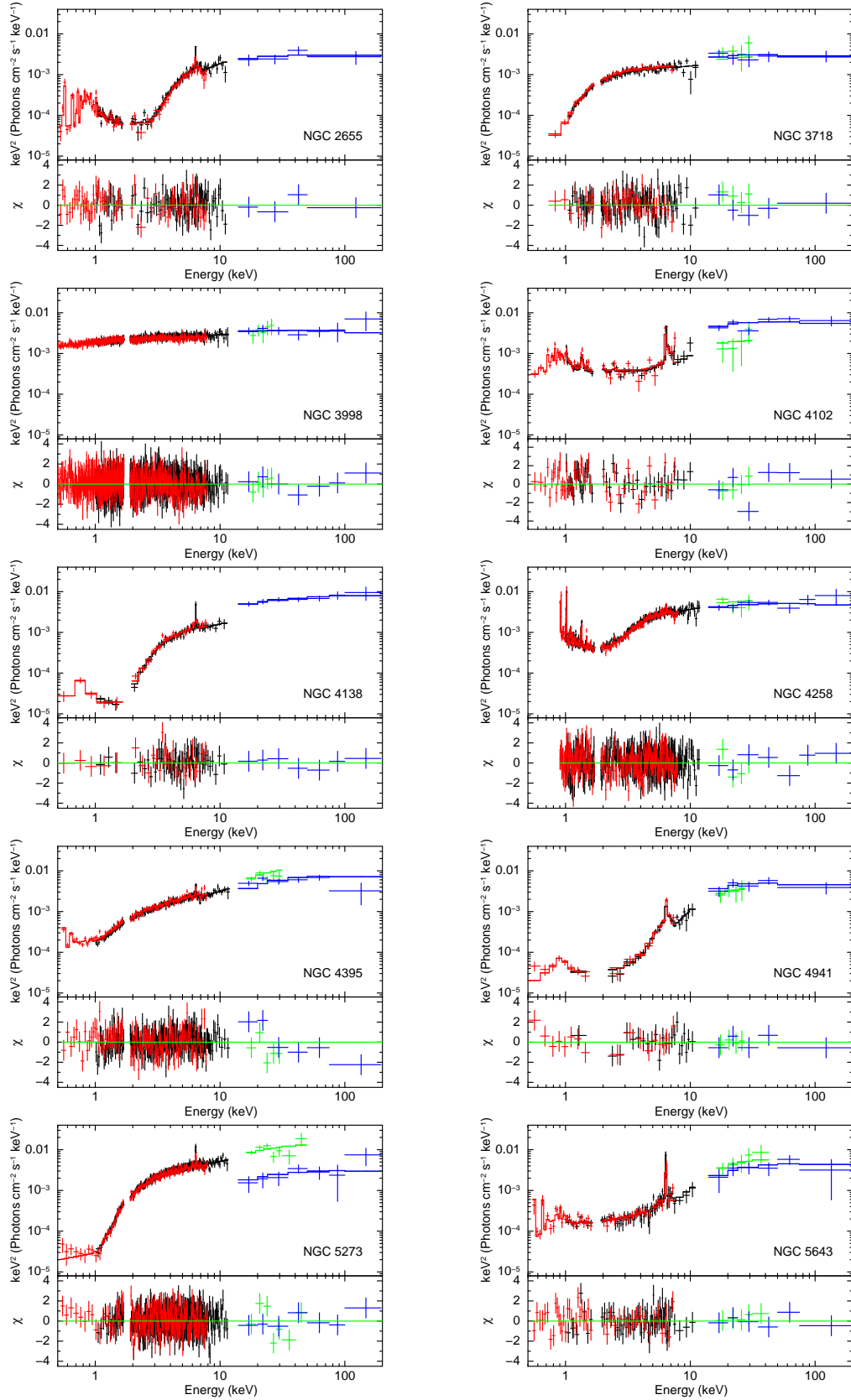


FIG. 2.— Unfolded *Suzaku* and *Swift*/BAT spectra. In the upper panels, the unfolded spectra of FI-XISs, BI-XIS, HXD/PIN, and *Swift*/BAT are represented with the black, red, green, and blue crosses, respectively. The solid curves show the best-fit model. In the lower panels, the residuals are shown.

which calculates a reflected spectrum from an optically

thick slab with a solid angle of Ω irradiated by a point

source (Magdziarz & Zdziarski 1995). We set the reflection strength, $R = \Omega/2\pi$, as a free parameter, and fix the inclination angle at 60° . It is confirmed that even if 30° is adopted, best-fit parameters do not significantly change. The shape of the incident spectrum is assumed to be the same as the power-law component. We basically assume that the reflection and scattered components did not vary between the *Suzaku* and *Swift*/BAT observations, considering that the size of the reflector has most likely a pc scale. In the three low mass LLAGNs (NGC 4395, NGC 5273, and NGC 5643), however, we assume that the reflection component varied in accordance with the primary emission because of a smaller size of the emitting regions. Thus, in these targets, R is defined with respect to the primary component in the *Suzaku* data. The **zgauss** component represents an iron-K α fluorescence line. The line width is fixed at 20 eV, which corresponds to a typical velocity dispersion of $\sim 2000 \text{ km s}^{-1}$ measured with *Chandra*/HETGS in local Seyfert galaxies (Shu et al. 2010). We always consider the Galactic absorption ($N_{\text{H}}^{\text{gal}}$), which is calculated with the **nh** command (Kalberla et al. 2005) in FTOOLS.

The details of the spectral analysis for individual targets are described in Section 3.2. The best-fit parameters, observed fluxes, and absorption corrected luminosities are summarized in Tables 4 and 5. The unfolded spectra and best-fit models are plotted in Figure 2 and 3. The Eddington ratios in Table 5 are calculated from the luminosity in the 2–10 keV band measured with *Suzaku* (*Swift*) for the low (high) mass LLAGNs, by assuming a bolometric correction factor of 10 (Ho 2009; Vasudevan et al. 2009).

3.2. Notes on Individual Objects

3.2.1. NGC 2655

For NGC 2655, the base-line model alone does not give an acceptable fit, leaving residuals in the soft X-ray band below 2 keV. Although one **apec** component is insufficient to improve the fit ($\chi^2/d.o.f = 226.4/169$), adding a second **apec** model gives an acceptable fit ($\chi^2/d.o.f = 186.6/167$). We obtain a hydrogen column density of $N_{\text{H}} = 2.61^{+0.27}_{-0.17} \times 10^{23} \text{ cm}^{-2}$ and $\Gamma = 1.77^{+0.19}_{-0.07}$, which are consistent with the *ASCA* result by Terashima et al. (2002). The temperatures of the **apec** models are $0.18^{+0.06}_{-0.05} \text{ keV}$ and $0.74 \pm 0.04 \text{ keV}$. The higher temperature is consistent with the *XMM-Newton* result (González-Martín et al. 2009). Although the lower temperature component has not been reported for this source, the value is within a range observed in nearby Seyfert galaxies (e.g., Cappi et al. 2006).

We significantly detect an iron-K α line at 6.4 keV, which was not detected in the previous *ASCA* and *XMM-Newton* observations (Terashima et al. 2002; González-Martín et al. 2009). The iron-K α line fluxes observed with *ASCA*, *XMM-Newton*, and *Suzaku* were $< 4.9 \times 10^{-6} \text{ photons s}^{-1} \text{ cm}^{-2}$, $< 3.3 \times 10^{-6} \text{ photons s}^{-1} \text{ cm}^{-2}$, and $5.3 \pm 1.2 \times 10^{-6} \text{ photons s}^{-1} \text{ cm}^{-2}$, respectively. Hence, the iron line flux slightly increased in the *Suzaku* observation (performed in 2014) compared with the *XMM-Newton* epoch (2005). This indicates that the spatial size of the reflector (torus) is less than a few pc.

3.2.2. NGC 3718

The base-line model well reproduces the X-ray spectra of NGC 3718, yielding $\chi^2/d.o.f = 214.9/206$ with $N_{\text{H}} = 1.29^{+0.12}_{-0.11} \times 10^{22} \text{ cm}^{-2}$ and $\Gamma = 1.86^{+0.13}_{-0.09}$. No significant iron-K α line is detected. Hernández-García et al. (2014) also reported a similar result by analyzing the *Chandra* and *XMM-Newton* spectra.

3.2.3. NGC 3998

The base-line model without a scattering component well reproduces the spectra with $\chi^2/d.o.f = 950.8/982$. The obtained photon index, $\Gamma = 1.84 \pm 0.01$, is consistent with a previous study (Ptak et al. 2004). We find that the reflection strength is very weak with an upper limit of $R_{\text{torus}} < 0.10$. No significant iron-K α line emission is detected, either. These suggest that there is little surrounding matter around the nucleus.

3.2.4. NGC 4102

The spectra of NGC 4102 are complex, and cannot be fit with the base-line model alone. By including two **apec** models, we obtain a better fit with $\chi^2/d.o.f = 348.15/271$. Further, adding three narrow emission lines other than the neutral iron-K α line largely improves the fit ($\chi^2/d.o.f = 299.3/265$). Each line component improves the fit by $\Delta\chi^2 > 7$ for two degrees of freedom (center energy and normalization). We obtain the line energies of $1.36 \pm 0.02 \text{ keV}$, $6.75^{+0.03}_{-0.04} \text{ keV}$, and $7.11^{+0.18}_{-0.10} \text{ keV}$, which possibly correspond to Mg XI, slightly blue-shifted Fe XXV, and Fe K β lines, respectively. The reflection strength derived from the continuum fit is small, $R_{\text{torus}} < 0.14$, whereas the observed equivalent width of the iron-K α line is large ($\sim 900 \text{ eV}$). This implies that the reflector may not be Compton thick.

3.2.5. NGC 4138

The base-line model combined with a single **apec** model well reproduces the X-ray spectra of NGC 4138 with $\chi^2/d.o.f = 78.1/94$. The addition of the **apec** model improves the fit by $\Delta\chi^2 = 26.9$ for two degrees of freedom (temperature and normalization). We obtain $N_{\text{H}} = 7.82^{+0.72}_{-0.68} \times 10^{22} \text{ cm}^{-2}$ and $\Gamma = 1.59^{+0.17}_{-0.06}$, which are consistent with the result of the *XMM-Newton* observation in 2001 (Cappi et al. 2006).

3.2.6. NGC 4258

The BI-XIS spectrum of NGC 4258 below 0.9 keV shows highly complex line features, and therefore we exclude this energy band for our analysis. The base-line model combined with two **apec** models gives a good fit ($\chi^2/d.o.f = 640.8/573$), which is better than that with a single **apec** model ($\chi^2/d.o.f = 659.1/575$). The obtained N_{H} , Γ , and temperatures of the **apec** components are consistent with the results by Makishima et al. (1994) based on the *ASCA* observation in 1993. A significant narrow iron-K α line at 6.4 keV is detected in our *Suzaku* spectra. The observations with *Chandra* in 2000 and 2001 and *XMM-Newton* in 2006 revealed that the observed iron-K α line fluxes were variable (e.g., Young & Wilson 2004; Reynolds et al. 2009). Indeed, the *Chandra* spectra did not show the iron-K α emission line (Young & Wilson 2004). Also, analyzing the *Suzaku*

and *XMM-Newton* spectra, Reynolds et al. (2009) concluded that the narrow iron-K α emission was originated from the accretion disk because of its flux variability on time scales of 160 days. Hence, the iron line emitting region of NGC 4258 may not be distant cold matter or a dusty torus. This fact is also recognized when we statistically discuss the torus structure of LLAGNs in Section 4.3.3.

3.2.7. NGC 4395

The spectra of NGC 4395 are well reproduced with the base-line model plus a narrow absorption line at $6.90^{+0.08}_{-0.07}$ keV ($\chi^2/d.o.f = 332.7/354$). The absorption line improves the fit by $\Delta\chi^2 = 7.5$, and is consistent with Fe XXVI K α . We obtain $R_{\text{torus}} = 1.67^{+1.73}_{-0.92}$ by assuming that the fluxes of the reflected emission varied between the *Suzaku* and *Swift*/BAT spectra (see above). We note that without this assumption we would derive an unphysically large reflection strength, $R_{\text{torus}} \sim 3.5$, which is much larger than typical values of $R_{\text{torus}} \sim 1$ observed in local AGNs (Dadina 2008).

3.2.8. NGC 4941

The base-line model plus an *apex* model well reproduces the spectra with $\chi^2/d.o.f = 33.1/43$. The broadband X-ray spectra were already analyzed by Kawamuro et al. (2013), and the difference from the previously used model is the absence of the disk-reflection component. The obtained parameters are consistent with each other.

3.2.9. NGC 5273

The base-line model gives a good fit with $\chi^2/d.o.f = 586.4/563$. The observed equivalent width of the iron-K α line, ~ 90 eV, is smaller than that estimated from the *XMM-Newton* data taken in 2002, ~ 230 eV (Capri et al. 2006), even though the observed continuum flux are almost the same. This suggests that the line emitting region must be smaller than a few pc and that the averaged past activity before each observation, which determines the iron-K α line flux, was higher in the earlier epoch. Similarly to the case of NGC 4395, we would obtain an unphysically large reflection strength of $R_{\text{torus}} \sim 5.7$ if we assumed that the reflection component did not change between the *Suzaku* and *Swift*/BAT observations.

3.2.10. NGC 5643

XMM-Newton observations (Guainazzi et al. 2004; Matt et al. 2013) showed that NGC 5643 contains a ULX, which is located at $\approx 0.9'$ from the nucleus and cannot be resolved with the *Suzaku* beamsize ($\approx 2'$). Because the nucleus is heavily obscured, the ULX emission may contaminate the XIS spectra at energies below 10 keV. Hence, we take into account the ULX spectrum (see Appendix) in our spectral analysis.

The base-line model plus the ULX component and two *apex* models well reproduces the spectra ($\chi^2/d.o.f = 109.5/114$). The large hydrogen column density of $N_{\text{H}} = 9.4^{+6.1}_{-3.2} \times 10^{23} \text{ cm}^{-2}$ and strong reflection strength of $R_{\text{torus}} \sim 0.9$ confirm that NGC 5643 has a heavily obscured AGN. We obtain an (apparent) scattered fraction of $f_{\text{scatt}} = 10.1^{+23.2}_{-7.4}\%$, although it strongly depends on

the assumed flux level of the ULX. When we increase the ULX flux by a factor of 2 to make it consistent with that measured by the *XMM-Newton* observation in 2003 (Guainazzi et al. 2004), we obtain only an upper limit of $f_{\text{scatt}} \lesssim 1\%$.

Our data can be used to constrain the variability of the ULX if we assume that the AGN is less variable. The summed 2–10 keV flux from the nucleus and ULX as observed with *Suzaku* in 2007 was $1.3 \times 10^{-12} \text{ erg s}^{-1} \text{ cm}^{-2}$, while the fluxes from the nucleus measured with *XMM-Newton* in 2003 and 2009 were both $\approx 8 \times 10^{-13} \text{ erg s}^{-1} \text{ cm}^{-2}$ (Guainazzi et al. 2004; Matt et al. 2013). By assuming that the flux from the nucleus remained constant, the ULX flux during the *Suzaku* observation is estimated to be $\approx 5 \times 10^{-13} \text{ erg s}^{-1}$. This value is between that during the *XMM-Newton* observation in 2003 ($7.5 \times 10^{-13} \text{ erg s}^{-1} \text{ cm}^{-2}$) and that in 2009 ($\sim 3.5 \times 10^{-13} \text{ erg s}^{-1} \text{ cm}^{-2}$), implying a consistent decay of the ULX flux from 2003 to 2009.

3.3. Broad Iron-K α Line

In this section, we investigate possible contribution of a relativistically broadened iron-K α line in our spectra. We exclude NGC 4102, NGC 4941, and NGC 5643 from this study, which show heavy absorptions ($N_{\text{H}} > 5 \times 10^{23} \text{ cm}^{-2}$) preventing detailed studies of the broad iron-K α line feature.

First, we fit the broadband X-ray spectra with the best-fit model obtained in Section 3.2 plus a disk-reflection component (*rdblur***pexmon*). The *rdblur* model calculates the relativistic blurring around a Schwarzschild black hole (Fabian et al. 1989), and the *pexmon* model reproduces the same reflection continuum as *pexrav* together with emission lines of Fe K α , Fe K β , and Ni K α computed in a self-consistent way (Nandra et al. 2007). This disk component is corrected for the same absorption and time variability as those for the primary X-ray emission. Because the two reflection components from the disk and distant matter are strongly coupled in a spectral fit, we fix the disk reflection strength R_{disk} . For this purpose, we refer to the study by George & Fabian (1991), who calculated the predicted equivalent width of the iron-K α line from an annulus slab irradiated by a point source with a power-law spectrum. We thus determine R_{disk} in the *pexmon* model that reproduces the predicted equivalent width of the iron-K α line, by assuming an inclination angle (θ_{inc}), a photon index, and a ratio between the scale height of the X-ray source and the inner radius of the annulus slab (r_{in}). Here θ_{inc} is set to 30° and 60° for type-1 ($N_{\text{H}} < 10^{22} \text{ cm}^{-2}$) and type-2 ($N_{\text{H}} > 10^{22} \text{ cm}^{-2}$) AGNs, respectively. For NGC 4258, we adopt $\theta_{\text{inc}} = 80^\circ$, which was precisely estimated by Maser observations (Herrnstein et al. 1999). The photon index is tied to that of the primary X-ray component. We adopt the scale height of $10r_{\text{g}}$ (r_{g} is the gravitational radius), a typical value measured in some AGNs (e.g., Morgan et al. 2008; Morgan et al. 2012). Then, we consider two cases, $r_{\text{in}} = 10r_{\text{g}}$ and $100r_{\text{g}}$, which correspond to $R_{\text{disk}} \simeq 0.6$ and $R_{\text{disk}} \simeq 0.1$, respectively. In the *rdblur* model, the outer radius and radial emissivity index are set to $r_{\text{out}} = 10^5 r_{\text{g}}$ and $\beta = -3$, respectively.

We find that adding the disk reflection component with the above parameters does not significantly improve the

TABLE 4
BEST-FIT PARAMETERS OBTAINED FROM BROADBAND X-RAY SPECTRAL ANALYSIS

Target Name	$N_{\text{H}}^{\text{Gal},*}$	N_{H}	N_{XIS}	Γ	f_{scat}	R_{torus}	$A_{\text{K}\alpha}$	kT	kT_2	$\chi^2/d.o.f.$
(1)	(2)	(3)	(4)	(5)	(6)	(7)	(8)	(9)	(10)	(11)
NGC 2655	2.18	$26.1^{+2.7}_{-1.7}$	$1.05^{+0.94}_{-0.23}$	$1.77^{+0.19}_{-0.07}$	$3.5^{+3.4}_{-1.4}$	$0.06(< 1.71)$	5.3 ± 1.2	$0.18^{+0.06}_{-0.05}$	0.74 ± 0.04	186.6/167
NGC 3718	1.06	$1.29^{+0.12}_{-0.11}$	$0.68^{+0.31}_{-0.15}$	$1.86^{+0.13}_{-0.09}$	$1.5^{+1.0}_{-0.7}$	$0.37(< 1.57)$	< 0.7	-	-	214.9/206
NGC 3998	1.01	$0.008^{+0.006}_{-0.005}$	$0.88^{+0.16}_{-0.12}$	1.84 ± 0.01	-	< 0.10	< 0.7	-	-	950.8/982
NGC 4102	1.68	81^{+34}_{-27}	$0.25^{+0.14}_{-0.12}$	$1.84^{+0.05}_{-0.13}$	$8.3^{+3.6}_{-2.3}$	< 0.14	14.7 ± 2.7	$0.61^{+0.11}_{-0.18}$	$1.10^{+0.18}_{-0.13}$	299.3/265
NGC 4138	1.25	$7.82^{+0.72}_{-0.68}$	$0.42^{+0.13}_{-0.09}$	$1.59^{+0.17}_{-0.06}$	$0.82^{+0.52}_{-0.39}$	$0.06(< 0.81)$	6.1 ± 1.5	$0.33^{+0.19}_{-0.06}$	-	78.1/94
NGC 4258	1.60	$12.10^{+0.52}_{-0.51}$	$1.07^{+0.37}_{-0.15}$	$1.77^{+0.10}_{-0.06}$	$16.2^{+5.6}_{-3.3}$	$0.07(< 0.86)$	$2.5^{+1.2}_{-1.1}$	$0.34^{+0.02}_{-0.03}$	$0.86^{+0.05}_{-0.07}$	640.8/573
NGC 4395	1.85	$1.55^{+0.28}_{-0.23}$	$1.55^{+0.28}_{-0.23}$	$1.49^{+0.15}_{-0.10}$	40^{+11}_{-9}	$1.67^{+1.73}_{-0.92}$	4.0 ± 1.2	0.19 ± 0.03	-	332.7/354
NGC 4941	2.17	70^{+17}_{-14}	$0.54^{+0.33}_{-0.18}$	$1.82^{+0.25}_{-0.26}$	$0.94^{+1.59}_{-0.60}$	$0.42^{+0.47}_{-0.26}$	6.2 ± 1.1	$0.87^{+0.14}_{-0.16}$	-	33.1/43
NGC 5273	0.916	$2.60^{+0.12}_{-0.11}$	$4.10^{+1.36}_{-0.85}$	$1.57^{+0.07}_{-0.06}$	$6.6^{+2.6}_{-1.7}$	$0.44^{+0.45}_{-0.35}$	9.7 ± 1.7	-	-	586.4/563
NGC 5643	8.01	94^{+61}_{-32}	$1.18^{+0.81}_{-0.48}$	$1.57^{+0.37}_{-0.31}$	$10.1^{+23.2}_{-7.4}$	$0.86(< 3.52)$	19.2 ± 2.1	0.18 ± 0.04	0.88 ± 0.14	109.5/114

NOTE. — Columns: (1) Galaxy name. (2) Galactic absorption in units of 10^{20} cm^{-2} . (3) Intrinsic absorption in units of 10^{22} cm^{-2} . (4) Normalization ratio of the primary X-ray emission in the *Suzaku*/FI-XISs spectrum to the *Swift*/BAT one. (5) Photon index of the power-law component. (6) Scattering fraction in units of %. (7) Relative reflection strength ($R = \Omega/2\pi$) of the *pexrav* model. (8) Photon flux of the *zgauss* model in units of $10^{-6} \text{ photons cm}^{-2} \text{ s}^{-1}$. (9)-(10) Temperatures of the *apec* models. (11) Reduced chi-squared over degrees of freedom.

* The parameter is fixed.

TABLE 5
FLUXES AND LUMINOSITIES

Target Name	$F_{0.5-2}^{\text{BI-XIS}}$	$F_{2-10}^{\text{FI-XISs}}$	$F_{10-50}^{\text{PIN},*}$	F_{10-50}^{BAT}	$L_{0.5-2}^{\text{BI-XIS}}$	$L_{2-10}^{\text{FI-XISs}}$	$L_{10-50}^{\text{PIN},*}$	L_{10-50}^{BAT}	$\log \lambda_{\text{Edd}}$
(1)	(2)	(3)	(4)	(5)	(6)	(7)	(8)	(9)	(10)
NGC 2655	3.1×10^{-13}	2.0×10^{-12}	-	6.8×10^{-12}	2.4×10^{41}	3.9×10^{41}	-	5.1×10^{41}	-3.2
NGC 3718	4.5×10^{-13}	3.3×10^{-12}	5.4×10^{-12}	7.3×10^{-12}	9.4×10^{40}	1.3×10^{41}	1.9×10^{41}	2.5×10^{41}	-3.8
NGC 3998	4.1×10^{-12}	6.6×10^{-12}	8.0×10^{-12}	9.1×10^{-12}	2.0×10^{41}	3.0×10^{41}	3.6×10^{41}	4.1×10^{41}	-4.5
NGC 4102	1.2×10^{-12}	1.5×10^{-12}	4.0×10^{-12}	1.3×10^{-11}	1.5×10^{41}	1.8×10^{41}	2.0×10^{41}	6.5×10^{41}	-3.3
NGC 4138	7.3×10^{-14}	2.2×10^{-12}	-	1.4×10^{-11}	5.0×10^{40}	1.0×10^{41}	-	4.4×10^{41}	-2.9
NGC 4258	2.5×10^{-12}	5.2×10^{-12}	1.2×10^{-11}	1.2×10^{-11}	5.1×10^{40}	6.3×10^{40}	8.7×10^{40}	8.2×10^{40}	-3.9
NGC 4395	6.9×10^{-13}	4.7×10^{-12}	1.8×10^{-11}	1.2×10^{-11}	3.9×10^{39}	9.4×10^{39}	3.3×10^{40}	2.3×10^{40}	-2.7
NGC 4941	8.4×10^{-14}	8.3×10^{-13}	6.7×10^{-12}	1.0×10^{-11}	1.4×10^{41}	2.1×10^{41}	3.4×10^{41}	5.5×10^{41}	-2.4
NGC 5273	3.1×10^{-13}	8.1×10^{-12}	2.2×10^{-11}	5.6×10^{-12}	8.4×10^{40}	2.0×10^{41}	4.5×10^{41}	1.1×10^{41}	-2.5
NGC 5643	4.4×10^{-13}	1.3×10^{-12}	9.0×10^{-12}	7.7×10^{-12}	6.6×10^{40}	1.3×10^{41}	3.3×10^{41}	2.8×10^{41}	-2.3

NOTE. — (1) Galaxy name. (2)–(5) Observed fluxes in the 0.5–2 keV (BI-XIS), 2–10 keV (FI-XISs), 10–50 keV (PIN), and 10–50 keV (BAT) bands. (6)–(9) Absorption-corrected luminosities in the 0.5–2 keV (BI-XIS), 2–10 keV (FI-XISs), 10–50 keV (PIN), and 10–50 keV (BAT) bands. (10) Eddington ratio.

* According to the XIS or HXD nominal positions, the fluxes and luminosities are divided by 1.16 or 1.18 to take into account the instrumental cross-calibration factor between FI-XISs and HXD/PIN.

fit in all 7 objects ($\Delta\chi^2 < 3$). Thus, our data do not require a cold standard disk extending down to $10\text{--}100 r_{\text{g}}$, although its presence cannot be strictly ruled out within the quality of our data (see below).

To derive upper limits of the flux of a broad iron-K α line, we replace *pexmon*rdblur* with *diskline+pexrav*rdblur* and fit the XIS spectra in the 3–9 keV (3–8 keV for BI-XIS) band. The parameters (θ_{inc} , β , r_{in} , and r_{out}) of the *diskline* model are set to the same as in the *rdblur* model. We leave the normalizations of the *zgauss*, *diskline*, and *zpowerlw* models as free parameters. Table 6 summarizes the line fluxes and equivalent widths ($\text{EW}_{\text{disk}}^{\text{obs}}$) of the broad iron-K α line in the case of $r_{\text{in}} = 10r_{\text{g}}$, which gives more conservative upper limits than the case of $r_{\text{in}} = 100r_{\text{g}}$. To check whether the assumed equivalent widths based on George & Fabian (1991) are consistent with the observed upper limits, we also calculate the corrected equivalent width ($\text{EW}_{\text{disk}}^{\text{cor}}$) with respect to the continuum composed of the primary power-law and disk-reflection components. We find that in NGC 3998

the upper limit of $\text{EW}_{\text{disk}}^{\text{cor}} < 20 \text{ eV}$ is inconsistent with the assumed one ($\approx 120 \text{ eV}$ for $r_{\text{in}} = 10r_{\text{g}}$ and $\approx 20\text{--}30 \text{ eV}$ for $r_{\text{in}} = 100r_{\text{g}}$), implying that the inner disk radius may be much larger than $100r_{\text{g}}$. In the other objects, the assumed equivalent widths are consistent within the observed upper limits, and hence the possible presence of a cold standard disk with $r_{\text{in}} = 10\text{--}100 r_{\text{g}}$ is not ruled out.

3.4. Narrow Iron-K α Line

Similarly, we obtain the flux and observed equivalent width of the narrow iron-K α line ($\text{EW}_{\text{gauss}}^{\text{obs}}$) by fitting the XIS narrow band (3–9 keV) spectra with the best-fit models obtained in Section 3.2. Only the normalizations of the *zgauss* and *zpowerlw* components are allowed to vary in this analysis. Figure 4 plots the spectra with the best-fit model. For easier comparison with model predictions (see Section 4.3.1), we also calculate the corrected equivalent width ($\text{EW}_{\text{gauss}}^{\text{cor}}$) with respect to the continuum composed of the primary power-law and torus-reflection components. The results are summarized

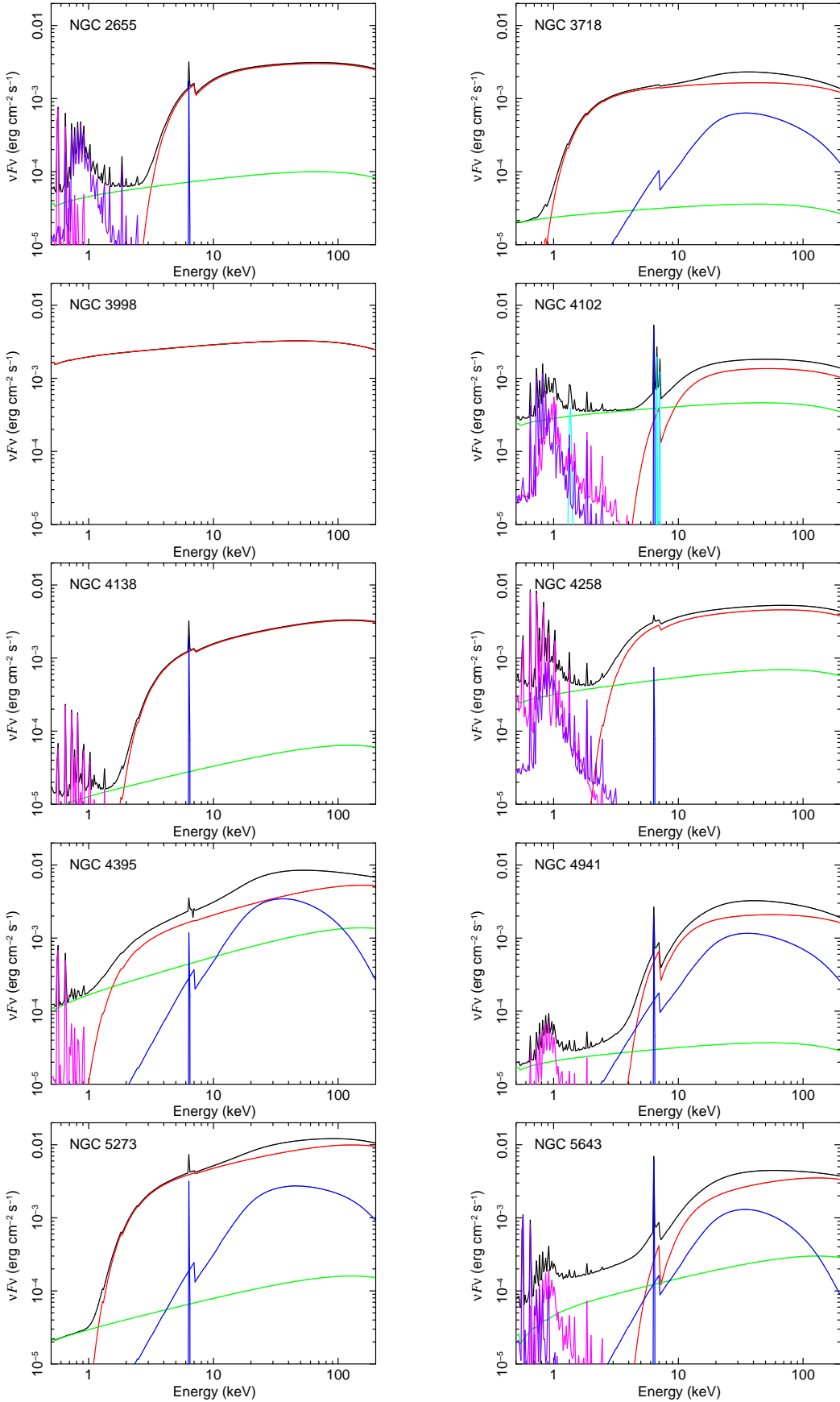


FIG. 3.— Best-fit models in units of νF_ν . The black, red, green, blue, and cyan lines correspond to the total, transmitted emission, scattered component, reflection components from the torus, and other emission lines than the iron-K α line, respectively. The purple and magenta lines represent the optically-thin thermal emission.

TABLE 6
FLUX AND EQUIVALENT WIDTHS OF BROAD
IRON-K α LINE

Target Name	N_{disk}	$\text{EW}_{\text{disk}}^{\text{obs}}$	$\text{EW}_{\text{disk}}^{\text{cor}}$
(1)	(2)	(3)	(4)
NGC 2655	< 12.2	< 250	< 300
NGC 3718	< 4.4	< 90	< 90
NGC 3998	< 0.9	< 20	< 20
NGC 4138	< 17.7	< 240	< 250
NGC 4258	< 9.3	< 100	< 130
NGC 4395	< 5.6	< 140	< 200
NGC 5273	< 2.1	< 80	< 80

NOTE. — (1) Galaxy name. (2) Photon flux of the **diskline** model in units of 10^{-6} photons $\text{cm}^{-2} \text{s}^{-1}$. (3) Observed equivalent width of the **diskline** model in units of eV. (4) Corrected equivalent width of the **diskline** model in units of eV.

TABLE 7
FLUX AND EQUIVALENT WIDTHS OF NARROW IRON-K α
LINE

Target Name	N_{gauss}	$\text{EW}_{\text{gauss}}^{\text{obs}}$	$\text{EW}_{\text{gauss}}^{\text{cor}}$
(1)	(2)	(3)	(4)
NGC 2655	5.3 ± 1.2	150 ± 30	160 ± 40
NGC 3718	< 0.7	< 20	< 20
NGC 3998	< 0.7	< 10	< 10
NGC 4102	$14.7^{+2.8}_{-2.7}$	920 ± 490	560 ± 300
NGC 4138	6.0 ± 1.5	190 ± 50	80 ± 20
NGC 4258	2.5 ± 1.2	30 ± 20	40 ± 20
NGC 4395	3.9 ± 1.2	70 ± 20	80 ± 20
NGC 4941	6.2 ± 1.1	380 ± 70	240 ± 50
NGC 5273	9.6 ± 1.7	90 ± 20	100 ± 20
NGC 5643	19.0 ± 2.1	1160 ± 330	1970 ± 560

NOTE. — (1) Galaxy name. (2) Photon flux of the **zgauss** model in units of 10^{-6} photons $\text{cm}^{-2} \text{s}^{-1}$. (3) Observed equivalent width of the **zgauss** model in units of eV. (4) Corrected equivalent width of the **zgauss** model in units of eV.

in Table 7.

4. DISCUSSIONS

4.1. Summary of X-ray Spectral Analysis

We have systematically analyzed the broadband X-ray spectra in the 0.5–200 keV band of ten nearby LLAGNs observed with *Suzaku* and *Swift*/BAT. The spectra are basically well reproduced with the base-line model composed of absorbed primary X-ray emission, a scattered component, and a reflection component from distant matter with a fluorescence iron-K α line. Some spectra require additional components, such as optically-thin thermal emission and emission/absorption lines. The spectra of NGC 3718 and NGC 3998 show no narrow iron-K α line, whereas it is significantly detected in the other objects. In the following discussions, we refer to the X-ray luminosities measured with *Suzaku* and *Swift*/BAT for the three low mass LLAGNs (NGC 4395, NGC 5273, and NGC 5643) and the other LLAGNs, respectively.

4.2. State of Accretion Disk

4.2.1. Broad Iron-K Line

In Section 3.3, we show that a relativistically broadened iron-K α line from a standard disk extending down to 10–100 r_g is not required from the spectral fit, even though we cannot, in most of the targets, rule out its presence within the statistical errors. Only upper limits of the line flux are derived. In the case of NGC 3998, the tight constraint on the equivalent width of the broad iron-K α line (< 20 eV) indicates that the standard disk must be truncated at a radius larger than $100r_g$. This is consistent with the result by Nemmen et al. (2014), who reported that a RIAF model fit to the SED of NGC 3998 requires a truncation radius larger than $1000r_g$.

4.2.2. Correlation between Photon Index and Eddington Ratio

The broadband coverage of our data including the hard X-ray band above 10 keV has enabled us to most reliably determine the photon index of the intrinsic power-law continuum even for obscured AGNs. Figure 5 plots the best-fit photon index against the Eddington ratio for our sample. We obtain a significant negative correlation with a form of $\Gamma = (-0.13 \pm 0.02) \log(\lambda_{\text{Edd}}) + (1.28 \pm 0.07)$ by a χ^2 fit (errors are 1σ). The slope is consistent with that found by Gu & Cao (2009), who derived a form of $\Gamma = (-0.09 \pm 0.03) \log(\lambda_{\text{Edd}}) + (1.55 \pm 0.07)$ for low Eddington-ratio ($\log \lambda_{\text{Edd}} \lesssim -2$) AGNs. Younes et al. (2011) also derived a negative but steeper slope of -0.31 ± 0.06 for lower Eddington-ratio AGNs ($\log \lambda_{\text{Edd}} < -3$). To compare our result with that of Gu & Cao (2009) in Figure 5, we convert the 2–10 keV luminosity into the bolometric one with a 2–10 keV bolometric correction factor of 10 (Ho 2009; Vasudevan et al. 2009).

It is known that the slope between the photon index and Eddington ratio turns into a positive value at high Eddington-ratio AGNs. For instance, Shemmer et al. (2008) reported a positive slope of 0.31 ± 0.01 for AGNs with $\log \lambda_{\text{Edd}} \gtrsim -2$. A similar result was also obtained by Brightman et al. (2013). As suggested by some authors (e.g., Shemmer et al. 2008; Gu & Cao 2009), the Γ - λ_{Edd} correlations for high and low Eddington-ratio AGNs imply that the state of the accretion disk changes according to the Eddington ratio. The positive correlation at the high Eddington-ratio regime can be explained in terms of standard disk as follows. A hot corona located above the disk produces Comptonized emission of seed photons provided from the disk. Hence, as the disk luminosity (or accretion rate) increases, electrons in the corona are more effectively cooled through inverse Compton scattering, leading to a smaller Compton y -parameter, and hence a softer spectrum. There are some numerical studies on the Γ - λ_{Edd} correlation for low Eddington-ratio AGNs under a RIAF assumption. For instance, the Convection dominated accretion flow model developed by Ball et al. (2001) predicts a negative correlation, whereas the Advection dominated accretion flow model by Narayan et al. (1998) predicts a positive one, which is inconsistent with the observations. Thus, this relation can be used to test RIAF models at low mass-accretion rates.

4.3. Torus Structure

4.3.1. Application of Torus Model

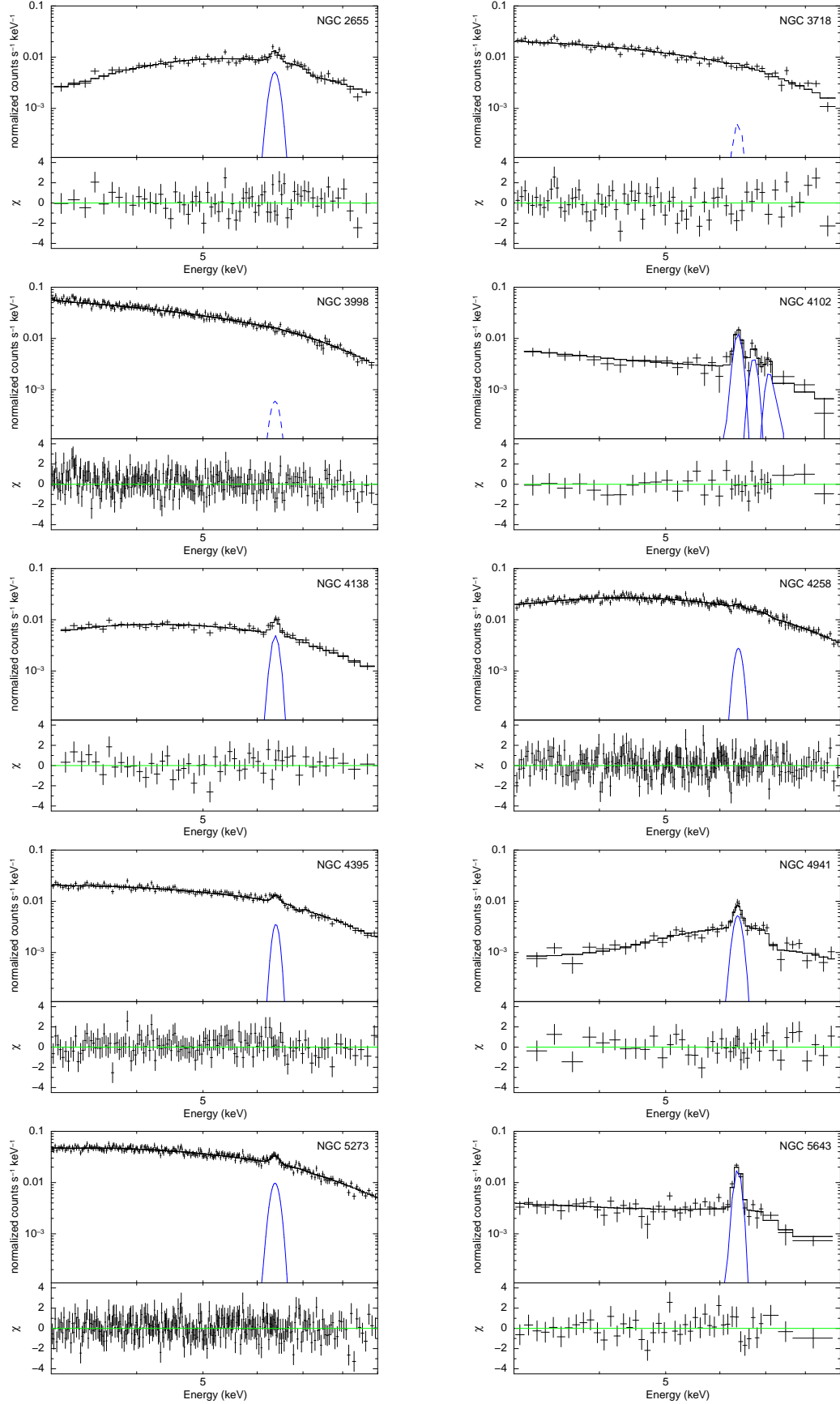


FIG. 4.— Spectra of FI-XISs in the 3–9 keV band. The black crosses and solid line represent the data and best-fit model, respectively. Emission lines that are detected significantly are shown with the blue solid lines, while those not significantly detected are shown with the blue dashed lines. The lower panel plots the residuals.

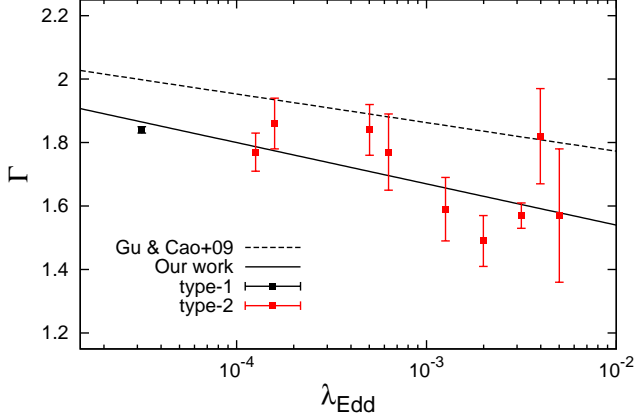


FIG. 5.— Photon index plotted against Eddington ratio. The solid line shows the best-fit correlation based on our sample, while the dashed line was derived by Gu & Cao (2009). Errors correspond to 1σ .

The flux (or equivalent width) of a narrow iron-K α line at 6.4 keV is useful to constrain the geometry and column density of circumnuclear matter, which we call the “torus”. To constrain the torus opening angle with respect to the polar axis, we utilize the Ikeda torus model (Ikeda et al. 2009), which is a Monte-Carlo based numerical spectral model. The torus structure has a nearly spherical shape with two conical-shaped holes along the rotation axis, and is defined by three parameters: the hydrogen column density at the equatorial plane (N_{H}^{eq}), the half opening angle (θ_{oa}), and the inclination angle (θ_{inc}). Hence, $\theta_{\text{inc}} < \theta_{\text{oa}}$ for type-1 AGNs and $\theta_{\text{inc}} > \theta_{\text{oa}}$ for type-2 AGNs. As done in previous works (Kawamuro et al. 2013; Tazaki et al. 2013), we fix N_{H}^{eq} at the observed line-of-sight column density (N_{H}) and a photon index of the incident X-ray spectrum according to the best-fit value listed in Table 4.

Figure 6 shows the predicted equivalent width of the iron-K α line as a function of θ_{oa} for several different inclinations. Because simulated spectra for $\theta_{\text{oa}} > 70^\circ$ are not available in the Ikeda torus model, for type-1 AGNs, we simply extrapolate the result at $\theta_{\text{oa}} = 70^\circ$ towards larger opening angles by assuming that the equivalent width is proportional to the volume of the torus. The observed range of $\text{EW}_{\text{gauss}}^{\text{cor}}$ at the 90% confidence limits is represented with the dot-dot-dot-dashed horizontal lines (magenta).

As noticed from Figure 6, the half opening angles of NGC 3718 and NGC 3998 cannot be constrained if we assume $N_{\text{H}}^{\text{eq}} = N_{\text{H}}$, although their weak iron-K α line fluxes and low line-of-sight absorptions suggest that their tori are little developed, having a small covering fraction and/or a small averaged column density. By contrast, NGC 2655, NGC 4102, NGC 4138, NGC 4258, and NGC 4941 have moderately developed tori, fulfilling $N_{\text{H}} > 7 \times 10^{22} \text{ cm}^{-2}$ and/or $\theta_{\text{oa}} < 70^\circ$. For NGC 4395, NGC 5273, and NGC 5643, the Ikeda model largely underpredicts the equivalent widths under the assumption of $N_{\text{H}}^{\text{eq}} = N_{\text{H}}$. We find that their equatorial hydrogen column densities must be larger than $6 \times 10^{22} \text{ cm}^{-2}$, $8 \times 10^{22} \text{ cm}^{-2}$, and $1.4 \times 10^{24} \text{ cm}^{-2}$, respectively, to consistently explain the observed values of $\text{EW}_{\text{gauss}}^{\text{cor}}$.

To summarize, we reveal that there are at least two types of LLAGNs in terms of torus structure: those with moderately developed tori ($\Omega/2\pi > 0.34$ corresponding to $\theta_{\text{oa}} < 70^\circ$, or $N_{\text{H}}^{\text{eq}} > 5 \times 10^{22} \text{ cm}^{-2}$) or those with little developed tori. The variety in the torus structure of LLAGNs is a new result obtainable only by detailed spectral analysis of individual objects. Previous works based on the type-2 AGN fraction have given only the “averaged” torus covering factor, which decreases towards lower luminosities (Burlon et al. 2011; Brightman & Nandra 2011).

4.3.2. Luminosity Dependence

Ricci et al. (2014) pointed out that, in order to discuss the torus structure of type-2 AGNs, the luminosity ratio between the iron-K α line and 10–50 keV continuum is a better indicator of the torus covering factor than the iron-K α equivalent width because the continuum flux above 10 keV is less affected by absorption than that at 6.4 keV. Using an AGN sample observed with *Suzaku*, they found that the $L_{\text{K}\alpha}/L_{10-50 \text{ keV}}$ ratio decreases with luminosity in both type-1 and type-2 AGNs at $L_{10-50 \text{ keV}} \gtrsim 10^{42} \text{ erg s}^{-1}$. These results can be explained if the torus covering fraction becomes smaller at higher luminosities, and are consistent with the anti-correlation between the absorbed-AGN fraction and luminosity in this luminosity range (e.g., Ueda et al. 2003).

We plot $L_{\text{K}\alpha}/L_{10-50 \text{ keV}}$ against luminosity of our LLAGN sample together with the original sample of Ricci et al. (2014) in Figure 7. Here we exclude Compton-thick AGNs ($N_{\text{H}} > 10^{24} \text{ cm}^{-2}$) because the heavy obscuration also strongly affects the iron-K α line flux and the relation may become complex (see Ricci et al. 2014). The dashed lines in the figure are the best-fit linear regression forms for type-1 and type-2 AGNs obtained by Ricci et al. (2014).

Figure 7 shows a trend that the $L_{\text{K}\alpha}/L_{10-50 \text{ keV}}$ ratio has a peak around $L_{10-50 \text{ keV}} = 10^{42} \text{ erg s}^{-1}$, from which the average value rapidly declines towards lower luminosities. This agrees with the implication from hard X-ray ($> 10 \text{ keV}$) surveys that the absorbed AGN fraction peaks at $\sim 10^{42-43} \text{ erg s}^{-1}$ and decreases with decreasing luminosity (Beckmann et al. 2009; Burlon et al. 2011). Thus, our study using the narrow iron-K α line supports the picture that the averaged solid angle of AGN tori is not a monotonically decreasing function with luminosity, and that irradiation is not the only key factor that determines the torus structure. We note that there is a large scatter of $L_{\text{K}\alpha}/L_{10-50 \text{ keV}}$ in the LLAGNs, as discussed in the previous subsection.

4.3.3. Eddington Ratio Dependence

Figure 8 shows the Eddington ratio dependence of $L_{\text{K}\alpha}/L_{10-50 \text{ keV}}$ based on our LLAGN sample. A positive correlation is seen between the $L_{\text{K}\alpha}/L_{10-50 \text{ keV}}$ ratio and λ_{Edd} . If we exclude NGC 4258 (the second left point), whose narrow iron-K α line may not be originated from the torus (Reynolds et al. 2009), there is a trend that all LLAGNs with $\lambda_{\text{Edd}} \lesssim 2 \times 10^{-4}$ have $L_{\text{K}\alpha}/L_{10-50 \text{ keV}}$ smaller than 10^{-3} . We thus infer that the Eddington ratio is a key parameter that affects the torus structure of LLAGNs: tori are hardly developed below a critical value of λ_{Edd} . Because the sample size is limited, however, we

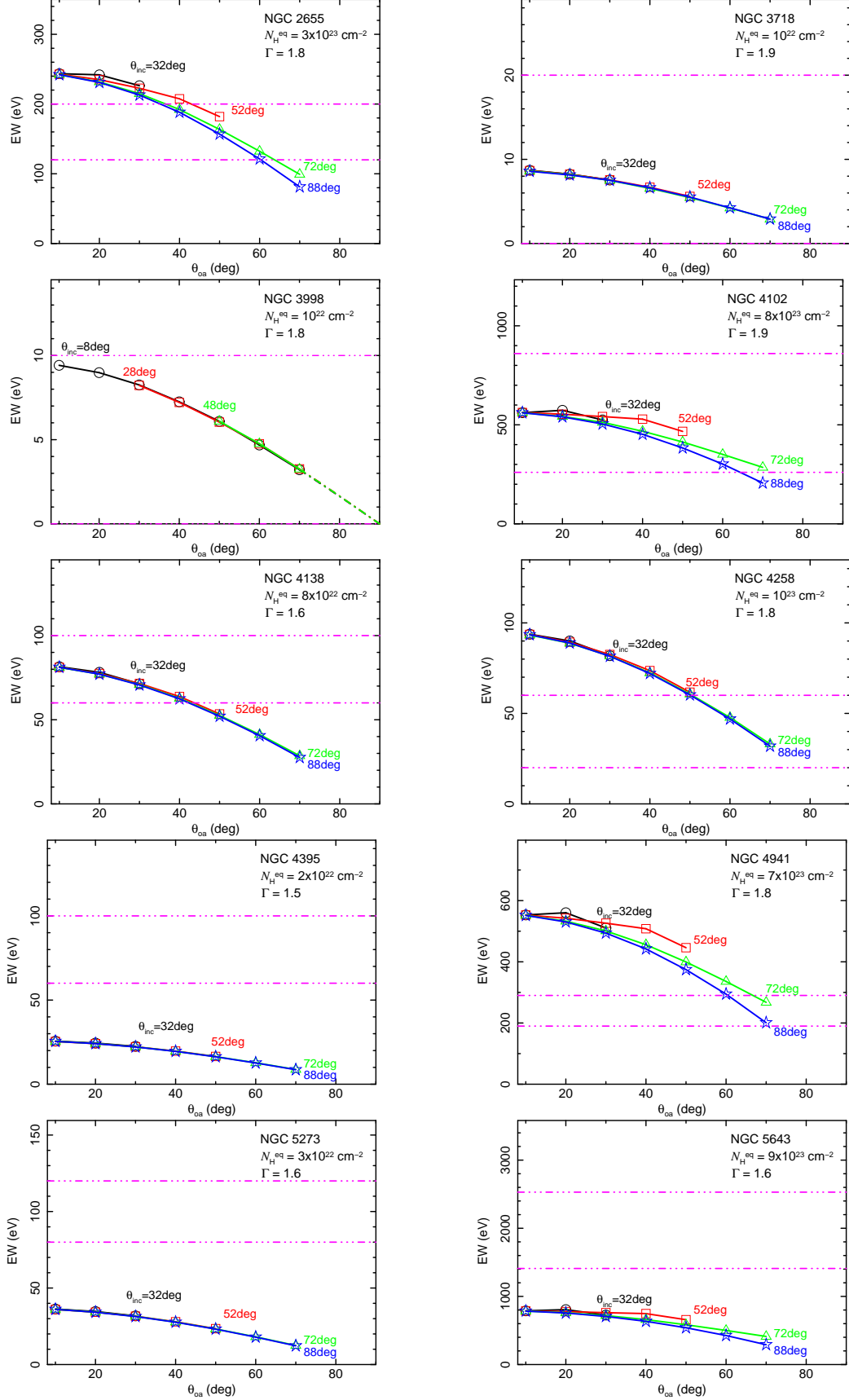


FIG. 6.— Predicted equivalent widths of the iron-K α line as a function of the torus half-opening angle with different inclinations, calculated from the torus model by Ikeda et al. (2009). The 90% confidence upper and lower limits of $\text{EW}_{\text{gauss}}^{\text{cor}}$ are represented with the two horizontal lines (magenta).

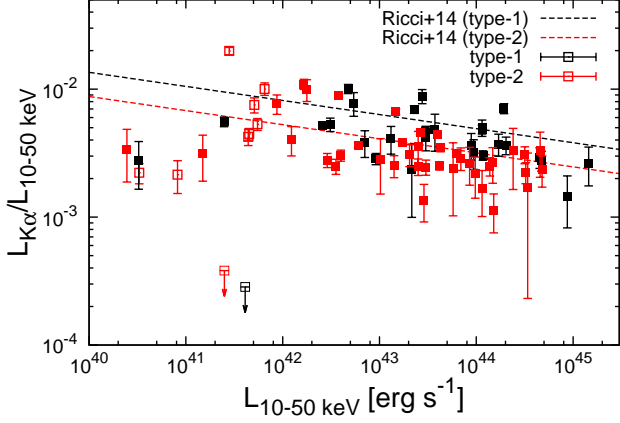


FIG. 7.— The luminosity ratio between the iron-K α line and 10–50 keV continuum plotted against the luminosity in the 10–50 keV band. The open squares are the data of our sample, while the filled ones are taken from Ricci et al. (2014). The arrows represent the upper limits for NGC 3718 and NGC 3998. The attached errors or upper limits are 1σ .

would need a larger number of LLAGNs to draw a robust conclusion. The lack of the torus may lead to the shortage of mass supply through it, hence reducing the mass-accretion rate. In an opposite way, the torus is not formed because of the lack of powerful outflow from the inner accretion disk at low mass-accretion rates. Thus, to understand the reason of the $L_{K\alpha}/L_{10-50\text{ keV}}$ versus λ_{Edd} correlation, we need to reveal the physical origin(s) of AGN tori.

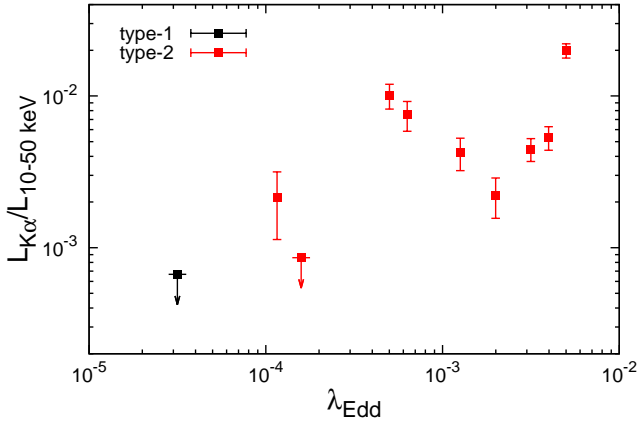


FIG. 8.— The luminosity ratio between the iron-K α line and 10–50 keV luminosity plotted against Eddington ratio for our LLAGN sample. The arrows represent the upper limits at the 90% confidence level for NGC 3718 and NGC 3998.

4.3.4. Correlation between Luminosities in X-ray and MIR Bands

Many studies found strong luminosity correlations between the X-ray and mid-infrared (MIR) bands (e.g., Lutz et al. 2004; Ramos Almeida et al. 2007; Gandhi et al. 2009; Asmus et al. 2011; Mason et al. 2012; Ichikawa et al. 2012; Asmus et al. 2015; Mateos et al. 2015; Stern 2015). Such correlation is expected because the dust torus heated by an AGN emits blackbody radiation in the MIR band.

Asmus et al. (2011) find no Eddington-ratio dependence of the X-ray/MIR (12 μm) luminosity ratio using a sample that covers a wide Eddington ratio range of $\log \lambda_{\text{Edd}} = -6 - 0$.

Figure 9 shows the L_X versus L_{MIR} correlation obtained from our LLAGN sample. The regression line derived by Asmus et al. (2015) from a large local AGN sample is plotted by the solid line. Asmus et al. (2015) took only the nuclear MIR emission by separating from that in the host galaxy, using subarcsecond resolution imaging data. We refer to the photometric data in the 12 μm band of Asmus et al. (2015) for our objects whenever available, and to the Wide-Field Infrared Survey Explorer (*WISE*) catalog (Wright et al. 2010) for the rest. Due to the poor angular resolution of *WISE* (6.5 arcsec), however, its flux may be contaminated from that of the host galaxy and hence should be regarded as an upper limit of the nuclear emission.

We find that our LLAGNs also approximately follow the same correlation as found by Asmus et al. (2015) for higher luminosity AGNs, regardless of AGN types and Eddington ratios. This is expected if a (moderate size of) torus is present in LLAGNs. There is a possibility that synchrotron emission from the jets or blackbody radiation from the truncated disk may contribute to the MIR luminosity in some LLAGNs (e.g., Ho 2008; Nemmen et al. 2014). Our result in Section 4.3.3 suggests that the low Eddington ratio LLAGNs ($\lambda_{\text{Edd}} \lesssim 2 \times 10^{-4}$) do not have developed tori. In these objects, the MIR luminosity would be indeed dominated by these emission mechanisms other than thermal emission from AGN-heated dust.

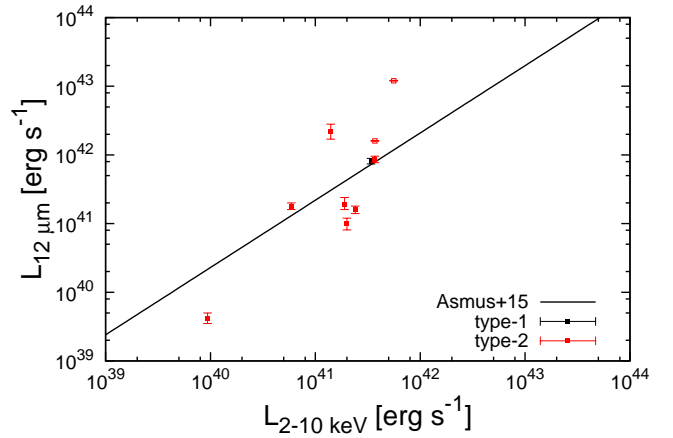


FIG. 9.— Luminosity correlation of our LLAGNs between the 12 μm and 2–10 keV bands. The solid line shows the regression line derived by Asmus et al. (2015). The 12 μm luminosities from the *WISE* catalog are represented with unfilled squares, while those taken from Asmus et al. (2015) with filled squares. Errors correspond to 1σ .

4.3.5. MIR Selection of LLAGNs

MIR SEDs are often used to identify AGNs by detecting a power-law component originating in AGN-heated dust (e.g., Polletta et al. 2007). The spectral index in the MIR band of luminous AGNs are typically $\alpha \lesssim -0.5$ in the form of $f_\nu = \nu^\alpha$ (e.g., Alonso-Herrero et al. 2006). Accordingly, Mateos et al. (2012) defined the so-called

AGN-wedge region in the MIR color-color diagram based on the three *WISE* bands ($3.4\ \mu\text{m}$, $4.6\ \mu\text{m}$, and $12.0\ \mu\text{m}$) in order to efficiently select luminous AGNs. Figure 10 shows the color-color plot of our LLAGN sample based on the *WISE* data together with the AGN-wedge region. As noticed, all objects are not located within this region. This is attributable to significant contamination from the host galaxy in the *WISE* MIR fluxes. This is an example demonstrating difficulty in identifying AGNs using MIR data alone.

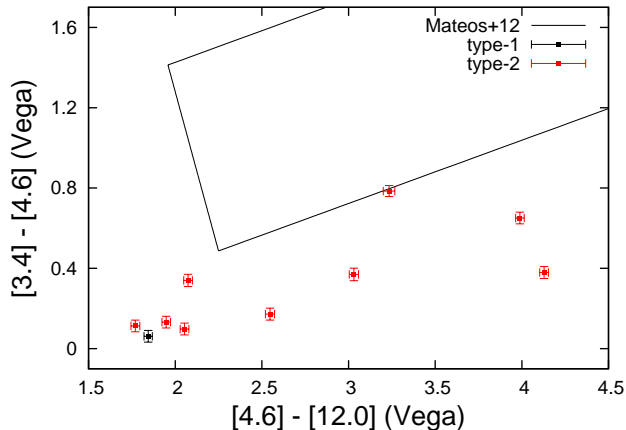


FIG. 10.— MIR color-color plot of our LLAGN sample, where the horizontal and vertical axes represent the $4.6\text{--}12.0\ \mu\text{m}$ and $3.4\text{--}4.6\ \mu\text{m}$ colors, respectively. The AGN wedge defined by Mateos et al. (2012) is surrounded by the solid lines. Errors correspond to 1σ .

5. CONCLUSIONS

We have performed a systematic broadband ($0.5\text{--}200\ \text{keV}$) X-ray spectral analysis of ten local LLAGNs (with intrinsic $14\text{--}195\ \text{keV}$ luminosities of $< 10^{42}\ \text{erg s}^{-1}$) observed with *Suzaku* and *Swift*/BAT. The main conclusions are summarized as follows.

1. The broadband X-ray spectra can be basically reproduced with an absorbed cut-off power law often accompanied by a reflection component from distant cold matter and a narrow fluorescence iron- $K\alpha$ line, and optically-thin thermal emission from the host galaxy.
2. In all objects, a relativistically blurred reflection component from a standard disk is not required from the spectra. We find the negative correlation between the photon index and Eddington ratio. These results are consistent with a picture that an optically-thin RIAF is formed at innermost radii in LLAGNs.
3. Applying a torus model by Ikeda et al. (2009), we find eight objects showing a significant narrow iron- $K\alpha$ emission line have a moderately developed torus with an equatorial column density of $\log N_{\text{H}}^{\text{eq}} > 22.7$ or a half opening-angle of $\theta_{\text{oa}} < 70^\circ$. The tori of the two LLAGNs without a narrow iron- $K\alpha$ line are likely little developed.
4. The luminosity ratio between the iron- $K\alpha$ line and $10\text{--}50\ \text{keV}$ continuum ($L_{K\alpha}/L_{10\text{--}50\ \text{keV}}$) has a peak

around $L_{10\text{--}50\ \text{keV}} = 10^{42}\ \text{erg s}^{-1}$, from which the average value rapidly declines towards lower luminosities. This result indicates that AGN irradiation is not the only key factor that determines the torus structure. Low Eddington-ratio LLAGNs with $\lambda_{\text{Edd}} \lesssim 2 \times 10^{-4}$ show small $L_{K\alpha}/L_{10\text{--}50\ \text{keV}}$ ratios. We infer that the Eddington ratio is a key parameter that affects the torus structure of LLAGNs.

5. Regardless of Eddington ratio, our LLAGNs follow the same luminosity correlation between the hard X-ray and MIR bands as found for more luminous AGNs. This implies that other emission mechanisms than AGN-heated dust are responsible for the MIR emission in low Eddington-ratio LLAGNs without developed tori.

We thank the referee for the comments, which helped us to improve the quality of the manuscript. We are grateful to C. Ricci for kindly providing us with the data. Part of this work was financially supported by the Grant-in-Aid for JSPS Fellows for young researchers (T.K) and for Scientific Research 26400228 (YU). This research has made use of the NASA/ IPAC Infrared Science Archive, which is operated by the Jet Propulsion Laboratory, California Institute of Technology, under contract with the National Aeronautics and Space Administration.

APPENDIX

XMM-NEWTON OBSERVATIONS OF THE ULX IN NGC 5643

To model the spectrum of the ULX in NGC 5643, we use the *XMM-Newton* data (OBSID = 0601420101) obtained in 2009, because the exposure ($\sim 50\ \text{ksec}$) is longer than that of the other *XMM-Newton* observation ($\sim 10\ \text{ksec}$) in 2003. The Standard Analysis Software (version 13.5.0) is utilized to reduce the data of the EPIC cameras (MOS-1, MOS-2, and pn). For all cameras, the source events are extracted from a circular region of a $26''$ radius, and the background events are taken from a source-free circular region with the same radius. The spectra of MOS-1 and MOS-2 are summed.

We find that a cut-off power law plus a disk-blackbody component well reproduces the spectra in the $0.3\text{--}7\ \text{keV}$ band ($\chi^2/d.o.f = 183.4/154$). Here the cut-off energy is fixed at $6\ \text{keV}$, a value observed from a typical ULX, NGC 1313 X-1 (Mizuno et al. 2007); the fit is not significantly improved by leaving the cut-off energy as a free parameter ($\chi^2/d.o.f = 182.4/153$). The best-fit parameters are a photon index of $\Gamma = 0.8$, a disk-blackbody normalization of $3.7 \times 10^{36}\ \text{erg s}^{-1}\ \text{kpc}^{-2}$, and a disk temperature of $0.35\ \text{keV}$. When we analyze the *Suzaku* spectra of NGC 5643, we always include this best-fit ULX model.

REFERENCES

- Alonso-Herrero, A., Pérez-González, P. G., Alexander, D. M., et al. 2006, *ApJ*, 640, 167
- Antonucci, R. 1993, *ARA&A*, 31, 473
- Asmus, D., Gandhi, P., Smette, A., Hönig, S. F., & Duschl, W. J. 2011, *A&A*, 536, A36
- Asmus, D., Gandhi, P., Hönig, S. F., Smette, A., & Duschl, W. J. 2015, *MNRAS*, 454, 766
- Ball, G. H., Narayan, R., & Quataert, E. 2001, *ApJ*, 552, 221
- Baumgartner, W. H., Tueller, J., Markwardt, C. B., et al. 2013, *ApJS*, 207, 19
- Bentz, M. C., Horenstein, D., Bazhaw, C., et al. 2014, *ApJ*, 796, 8
- Beckmann, V., Soldi, S., Ricci, C., et al. 2009, *A&A*, 505, 417
- Brightman, M., & Nandra, K. 2011, *MNRAS*, 414, 3084
- Brightman, M., Silverman, J. D., Mainieri, V., et al. 2013, *MNRAS*, 433, 2485
- Buchner, J., Georgakakis, A., Nandra, K., et al. 2015, *ApJ*, 802, 89
- Burlon, D., Ajello, M., Greiner, J., et al. 2011, *ApJ*, 728, 58
- Beifiori, A., Courteau, S., Corsini, E. M., & Zhu, Y. 2012, *MNRAS*, 419, 2497
- Cappi, M., Panessa, F., Bassani, L., et al. 2006, *A&A*, 446, 459
- Dadina, M. 2008, *A&A*, 485, 417
- Davis, B. L., Berrier, J. C., Johns, L., et al. 2014, *ApJ*, 789, 124
- Della Ceca, R., Caccianiga, A., Severgnini, P., et al. 2008, *A&A*, 487, 119
- den Brok, M., Seth, A. C., Barth, A. J., et al. 2015, *ApJ*, 809, 101
- Fabian, A. C., Rees, M. J., Stella, L., & White, N. E. 1989, *MNRAS*, 238, 729
- Fukazawa, Y., Mizuno, T., Watanabe, S., et al. 2009, *PASJ*, 61, 17
- Gandhi, P., Horst, H., Smette, A., et al. 2009, *A&A*, 502, 457
- George, I. M., & Fabian, A. C. 1991, *MNRAS*, 249, 352
- González-Martín, O., Masegosa, J., Márquez, I., Guainazzi, M., & Jiménez-Bailón, E. 2009, *A&A*, 506, 1107
- Gültekin, K., Richstone, D. O., Gebhardt, K., et al. 2009, *ApJ*, 698, 198
- Gu, M., & Cao, X. 2009, *MNRAS*, 399, 349
- Guainazzi, M., Mihara, T., Otani, C., & Matsuoka, M. 1996, *PASJ*, 48, 781
- Guainazzi, M., Rodríguez-Pascual, P., Fabian, A. C., Iwasawa, K., & Matt, G. 2004, *MNRAS*, 355, 297
- Gruber, D. E., Matteson, J. L., Peterson, L. E., & Jung, G. V. 1999, *ApJ*, 520, 124
- Hasinger, G. 2008, *A&A*, 490, 905
- Hernández-García, L., González-Martín, O., Masegosa, J., & Márquez, I. 2014, *A&A*, 569, A26
- Herrnstein, J. R., Moran, J. M., Greenhill, L. J., et al. 1999, *Nature*, 400, 539
- Ho, L. C. 2008, *ARA&A*, 46, 475
- Ho, L. C. 2009, *ApJ*, 699, 626
- Ho, L. C., Greene, J. E., Filippenko, A. V., & Sargent, W. L. W. 2009, *ApJS*, 183, 1
- Humphreys, E. M. L., Reid, M. J., Moran, J. M., Greenhill, L. J., & Argon, A. L. 2013, *ApJ*, 775, 13
- Ichikawa, K., Ueda, Y., Terashima, Y., et al. 2012, *ApJ*, 754, 45
- Ikeda, S., Awaki, H., & Terashima, Y. 2009, *ApJ*, 692, 608
- Kalberla, P. M. W., Burton, W. B., Hartmann, D., et al. 2005, *A&A*, 440, 775
- Kawamuro, T., Ueda, Y., Tazaki, F., & Terashima, Y. 2013, *ApJ*, 770, 157
- Kondratko, P. T., Greenhill, L. J., & Moran, J. M. 2005, *ApJ*, 618, 618
- Lawrence, A. 1991, *MNRAS*, 252, 586
- Lutz, D., Maiolino, R., Spoon, H. W. W., & Moorwood, A. F. M. 2004, *A&A*, 418, 465
- Magdziarz, P., & Zdziarski, A. A. 1995, *MNRAS*, 273, 837
- Makishima, K., Fujimoto, R., Ishisaki, Y., et al. 1994, *PASJ*, 46, L77
- Markakis, K., Dierkes, J., Eckart, A., et al. 2015, *A&A*, 580, A11
- Mason, R. E., Lopez-Rodriguez, E., Packham, C., et al. 2012, *AJ*, 144, 11
- Mateos, S., Alonso-Herrero, A., Carrera, F. J., et al. 2012, *MNRAS*, 426, 3271
- Mateos, S., Carrera, F. J., Alonso-Herrero, A., et al. 2015, *MNRAS*, 449, 1422
- Matt, G., Bianchi, S., Marinucci, A., et al. 2013, *A&A*, 556, A91
- Merloni, A., Bongiorno, A., Brusa, M., et al. 2014, *MNRAS*, 437, 3550
- Mitsuda, K., Bautz, M., Inoue, H., et al. 2007, *PASJ*, 59, 1
- Mizuno, T., Miyawaki, R., Ebisawa, K., et al. 2007, *PASJ*, 59, 257
- Morgan, C. W., Eyler, M. E., Kochanek, C. S., et al. 2008, *ApJ*, 676, 80
- Morgan, C. W., Hainline, L. J., Chen, B., et al. 2012, *ApJ*, 756, 52
- Nandra, K., O'Neill, P. M., George, I. M., & Reeves, J. N. 2007, *MNRAS*, 382, 194
- Narayan, R., Mahadevan, R., & Quataert, E. 1998, *Theory of Black Hole Accretion Disks*, 148
- Nemmen, R., Storchi-Bergmann, T., & Eracleous, M. 2011, *arXiv:1112.4640*
- Nemmen, R. S., Storchi-Bergmann, T., & Eracleous, M. 2014, *MNRAS*, 438, 2804
- Polletta, M., Tajer, M., Maraschi, L., et al. 2007, *ApJ*, 663, 81
- Pounds, K. A., Reeves, J. N., King, A. R., & Page, K. L. 2004, *MNRAS*, 350, 10
- Ptak, A., Terashima, Y., Ho, L. C., & Quataert, E. 2004, *ApJ*, 606, 173
- Quataert, E. 2001, *Probing the Physics of Active Galactic Nuclei*, 224, 71
- Ramos Almeida, C., Pérez García, A. M., Acosta-Pulido, J. A., & Rodríguez Espinosa, J. M. 2007, *AJ*, 134, 2006
- Reynolds, C. S., Nowak, M. A., Markoff, S., et al. 2009, *ApJ*, 691, 1159
- Ricci, C., Ueda, Y., Paltani, S., et al. 2014, *MNRAS*, 441, 3622
- Rodríguez-Pascual, P. M., Alloin, D., Clavel, J., et al. 1997, *ApJS*, 110, 9
- Shakura, N. I., & Sunyaev, R. A. 1973, *A&A*, 24, 337
- Shemmer, O., Brandt, W. N., Netzer, H., Maiolino, R., & Kaspi, S. 2008, *ApJ*, 682, 81
- Shu, X. W., Yaqoob, T., & Wang, J. X. 2010, *ApJS*, 187, 581
- Springob, C. M., Masters, K. L., Haynes, M. P., Giovanelli, R., & Marinoni, C. 2009, *ApJS*, 182, 474
- Stern, D. 2015, *ApJ*, 807, 129
- Tazaki, F., Ueda, Y., Terashima, Y., Mushotzky, R. F., & Tombesi, F. 2013, *ApJ*, 772, 38
- Terashima, Y., Iyomoto, N., Ho, L. C., & Ptak, A. F. 2002, *ApJS*, 139, 1
- Terashima, Y., Gallo, L. C., Inoue, H., et al. 2009, *PASJ*, 61, 299
- Theureau, G., Hanski, M. O., Coudreau, N., Hallet, N., & Martin, J.-M. 2007, *A&A*, 465, 71
- Tully, R. B., 1988, *Nearby Galaxies Catalog*. Cambridge Univ. Press, Cambridge
- Tully, R. B., Rizzi, L., Shaya, E. J., et al. 2009, *AJ*, 138, 323
- Ueda, Y., Akiyama, M., Ohta, K., & Miyaji, T. 2003, *ApJ*, 598, 886
- Ueda, Y., Akiyama, M., Hasinger, G., Miyaji, T., & Watson, M. G. 2014, *ApJ*, 786, 104
- Vasudevan, R. V., Mushotzky, R. F., Winter, L. M., & Fabian, A. C. 2009, *MNRAS*, 399, 1553
- Younes, G., Porquet, D., Sabra, B., & Reeves, J. N. 2011, *A&A*, 530, A149
- Young, A. J., & Wilson, A. S. 2004, *ApJ*, 601, 133
- Walsh, J. L., van den Bosch, R. C. E., Barth, A. J., & Sarzi, M. 2012, *ApJ*, 753, 79
- Wright, E. L., Eisenhardt, P. R. M., Mainzer, A. K., et al. 2010, *AJ*, 140, 1868